METHODS

Prediction of Photovoltaic (PV) Thermal Fault Location Using the Catadioptric Device

PUTU AGUS ADITYA PRAMANA [ID] **AND RINALDY DALIMI**

Department of Electrical Engineering, Universitas Indonesia, Depok, Jawa Barat 16424, Indonesia

Corresponding author: Rinaldy Dalimi (rinaldy@eng.ui.ac.id)

ABSTRACT Photovoltaic (PV) farms are subject to thermal faults that can degrade and reduce module efficiency. The currently used method of detecting thermal fault is time-consuming and hard to locate the fault position, especially in large PV areas. It can result in additional flaws, such as igniting the PV farm. We provide a new approach for monitoring and detecting PV thermal faults through a catadioptric device (CD) that offers fast and continual detection. As an early development stage, in this study, we concentrate on building a mathematical model that can determine the thermal fault coordinate based on two object images from different CD positions. The experiment then verifies the model, and the parameter variation is performed to find the coordinate prediction characteristic. Also, a case study simulation on large PV system monitoring was performed to figure out the thermal fault localization process. The result shows that the mathematical model can be used to determine the coordinate position of the thermal fault with acceptable measurement error. The parameter x_k tends to affect the average measurement error of the coordinate prediction and the error gradient of each axes couple. Greater the x_k, smaller measurement and gradient error can be achieved. In addition, the case study simulation result shows that the thermal fault position can be predicted with the worst percentage error (PE) of less than 10%, with a mean absolute percentage error (MAPE), mean absolute error (MAE), and root mean square error (RMSE) in a reasonable value. Also, the sensitivity pattern can be used for CD condition monitoring.

INDEX TERMS Thermal fault, PV, catadioptric, detection, localization.

I. INTRODUCTION

Environmental issues are a matter of concern for the world community today, especially the problem of global warming triggered by greenhouse gas emissions that result from burning fossil fuels, including for power generation. It encourages power generation technology to move in a more environmentally friendly direction, such as using photovoltaic (PV) [1]. PV is the leading choice for areas with significant enough irradiation because they are modular and easy to install. PV utilization globally has reached a value of 100GW and continues to grow along with the increasing demand for green energy [2].

PV is made of semiconductor materials composed of small components called cells. These small components are then

connected in series or parallel to obtain a PV module with the desired current and voltage specifications. Currently, many types of PV cell technology have different efficiency and prices [3].

In field operation, PV modules can experience various kinds of disturbances, such as encapsulant damage, cracking, delamination, connection failure, mismatch fault, corrosion, diode failure, and arc fault [4], [5], [6]. These disturbances can cause thermal problems, such as degrading and firing the PV farm [7], [8]. Therefore, the proper PV monitoring system is needed to maintain optimal PV performance [9], [10], [11], [12].

Various methods are proposed to detect thermal faults, including frequency analysis, electromagnetic induction, artificial intelligence, and thermal imaging [13], [14], [15], [16], [17]. However, thermal imaging is the most used. This method maps the PV module's temperature distribution into

images with different colors. The color in the thermal image looks very contrasting if there is a hotspot on the PV module. Hotspots on the PV module can reach temperatures of more than 100°C, so the hotspot points should be very clearly visible compared to normal cells [18], [19], [20].

The use of thermal cameras to detect thermal faults on PV in Indonesia is generally done manually. The process occurs when the operator inspects the PV module condition one by one. If there is a thermal fault on the module, the operator marks the module and then moves to another module to perform the same steps. After the locations of the modules experiencing thermal faults are mapped, maintenance planning is carried out for these modules. The manual method's thermal fault detection process requires the operator to move from one module to another. Therefore, monitoring the condition of the module is only in the form of sampling at certain times

In addition to the manual method carried out by the operator, a PV thermal fault detection method using drones has been developed in other countries. The drone is flown over the PV area and then records the image of the PV module with a thermal camera. After the image of one area is obtained, the drone moves to another to obtain a thermal image of the entire PV farm. Drones are flown at particular times scheduled for the maintenance process; outside these times, the thermal fault conditions on the PV cannot be monitored [11], [21], [22].

The previous method (manual and drone) are not continuously monitoring the PV module's condition. Besides, this method also takes a long time to detect thermal fault disturbances in the PV module. In PV with a capacity of 15MWp, it is estimated that there are around 60000 modules. Using the manual method, it takes about 105 days to map the overall condition of the module, while using a drone takes about 15 days. Both of these methods cannot monitor the occurrence of thermal faults on the PV module if it occurs outside the monitoring schedule, even though thermal fault disturbances can occur at certain times and disappear at other times. The emergence of thermal faults that occur repeatedly and are not detected by the monitoring system causes damage to the module and reduces the efficiency [23], [24], [25], and if the thermal fault occurs in the form of arcing, it can trigger fires in the PV module [7], [8], [26].

In addition to the applicable methods in the real world described above, there is also a method of detecting thermal disturbances in the research phase, namely the artificial intelligence (AI) method. In the AI method, the current and voltage signals from the PV are recorded, and then training is carried out. The results of this training are then used as the basis for determining the fault appearance of the PV module. However, the ability to determine fault coordinates was not discussed [27], [28].

The shortcomings of the previous method, which is noncontinuous monitoring and takes time to determine the fault location, are tried to face by the proposed method. This paper describes the thermal fault monitoring model using the catadioptric device (CD). The monitoring system model utilizes
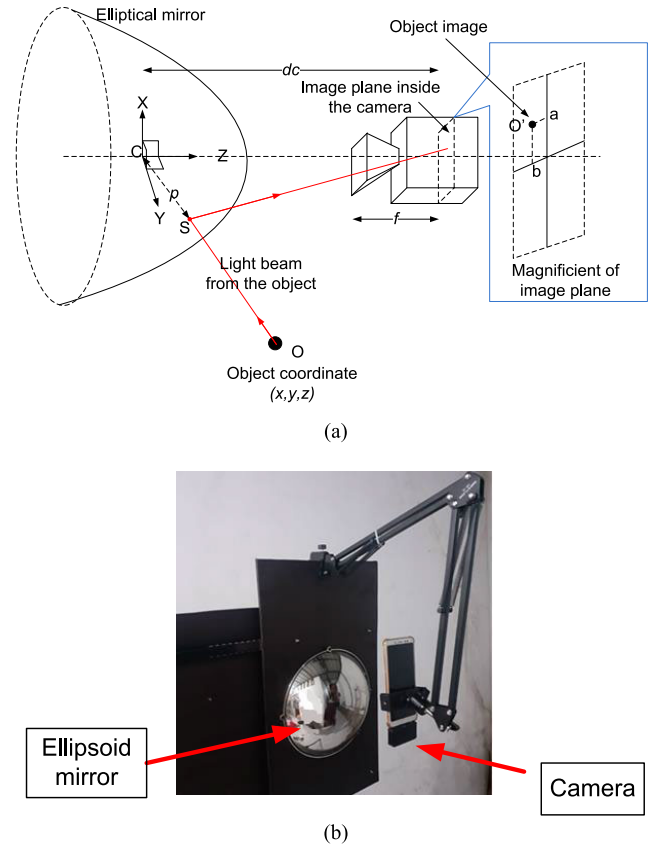

FIGURE 1. Catadioptric Device (CD). (a) Object image formation on the CD. (b) Experimental construction of CD.

the CD that contains an ellipsoid mirror and is mounted on a pole with a certain height. Using the CD with ellipsoid mirrors aims to produce a wide field of view [29]. With this, more modules can be monitored in one device so thermal fault detection can be carried out more effectively and efficiently.

It is a preliminary study to determine the coordinates of the thermal fault coordinate, so it focuses more on modelling and its verification, which also is fulfilled with one simulation case study. The presentation of this paper consists of four sections. Section I described the research background, including PV thermal fault problems, the gap in the existing detection method, and the use of CD to complete the previous method. The modelling process of coordinate prediction, including analysis and discussion, is explained in Section II. A case study of thermal fault localization in a large PV farm using simulation is given in Section III. Section IV is the conclusion.

II. DETERMINATION OF OBJECT COORDINATES

A CD is an optical device combining a mirror and a lens (camera). The concept is that the mirror captures and then projects the object image on its surface following its curvature. The lens then captures the image projected on the mirror surface. In this study, an ellipsoid mirror is utilized in the CD.

A. MODELING

Determining the coordinates of the thermal fault location on the PV is carried out first by modelling the formation of images on the CD, as given in Figure 1.

Figure 1(a) shows a catadioptric device consisting of an ellipsoid mirror and a camera. The ellipsoid mirror captures the light beam emitted by object O at coordinates (x,y,z) and projects the object's location at position S on the mirror surface. The camera receives the reflected light from the object in position S. The light from the object image in S received by the camera is then captured by the camera's internal sensor (image plane) and forms the image of the object O'. This object image then has coordinates (a,b) on the image plane, where the values are determined by (1) and (2) [30], [31]. e is the eccentricity of the mirror, f is the focal length of the camera, d_C is the distance between the mirror and the camera. p is the focal length of the ellipsoid mirror. $x, y,$ and z are the object coordinates relative to the mirror center. a and b represent the object image coordinates. Figure 1(b) shows the experimental construction of the CD used to perform the model verification in Figure 2.

$$\frac{epfx}{d_C\sqrt{x^2+y^2+z^2}+e(p+d_C)z}=a \tag{1}$$

$$\frac{epfy}{d_C\sqrt{x^2+y^2+z^2}+e(p+d_C)z}=b \tag{2}$$

In this case, the midpoint of CD is the coordinates (0,0,0). When CD experiences a shift in the x-direction of x_k, the object's coordinates relative to the position of CD are as in equation (3).

$$\begin{bmatrix} x \\ y \\ z \end{bmatrix} = \begin{bmatrix} x_0 + x_k \\ y_0 \\ z_0 \end{bmatrix} \tag{3}$$

If equation (1) is divided by equation (2), it is obtained equation (4).

$$\frac{a}{b}=\frac{x}{y} \tag{4}$$

By substituting equation (4) into equation (1), it is obtained equation (5)

$$\frac{k_2 y}{d_C\sqrt{k_4 y^2 + z^2}+k_3 z}=a \tag{5}$$

where :

$$k_2 = epf\frac{a}{b}$$
$$k_3 = e(p+d_c)$$
$$k_4 = \left(\frac{a^2}{b^2}+1\right)$$

By decomposing and grouping the variables in (5), it is obtained (6).

$$Ay^2 - Byz - Cz^2 = 0 \tag{6}$$

where :

$$A = \left(k_2^2 - a^2 d_c^2 k_4\right)$$
$$B = -2ak_2 k_3$$
$$C = -\left(a^2 d_c^2 - a^2 k_3^2\right)$$

By substituting the equations for x and y in (3) into (6), we get (7).

$$Ay_0^2 + By_0 z_0 + Cz_0^2 = 0 \tag{7}$$

The relationship between the actual coordinates of objects affected by the CD parameter is given in (7). In (7), one of the object's coordinates, namely the x-coordinate, has been eliminated so that the remaining two coordinate variables are the y-coordinate (in this case, y_0) and z-coordinate (in this case, z_0). Additional data is needed to find two variable values with one equation using two different conditions for each object whose location is determined.

In this case, the two conditions in question are using two accompanying CDs or using one CD but can move to another x-coordinate with the same height. The position of the CD that has shifted can cause a relative change in the values of x, y, z. To see the relationship between x and y, (3) is used by dividing x and y to obtain (8).

$$\frac{x}{y} = \frac{x_0 + x_k}{y_0} = \frac{a}{b}$$
$$bx_0 - ay_0 = -bx_k \tag{8}$$

Two image coordinates are obtained using two CD conditions: (a_0, b_0) and (a_k, b_k). If these two coordinates are entered into equation (8), then equations (9) and (10) are obtained as follows.

$$b_0 x_0 - a_0 y_0 = -b_0 x_0 \tag{9}$$
$$b_k x_0 - a_k y_0 = -b_k x_k \tag{10}$$

The process of elimination of y_0 in (9) and (10) to get the value of x_0 is carried out; equation (11) is obtained as follows.

$$x_0 = \frac{-b_k a_0 x_k + b_0 a_k x_0}{b_k a_0 - b_0 a_k} \tag{11}$$

The value of x_0 from (11) is then entered into (9) so that the value of y_0 is obtained. The value of y_0 is then substituted into (7) to get the value of z_0.

B. MODEL VERIFICATION

After obtaining a mathematical model to determine the object's coordinates, the formulation is verified by retrieving experimental data. The experimental scheme is given in Figure 2.

Figure 2 shows an illustration of the verification process. The CD has characteristics of $e = 0.5$, $dc=300$mm, and $p = 274$mm. Chromium-coated metal (as a mirror) ensures 90% visible light and infrared waves are reflected while the camera has a focal length of $f = 1.25$mm. The mathematical model is verified by placing ten square (length of 10cm) white color objects (Obj 1 to Obj 10 in Figure 2) in front of CD, whose
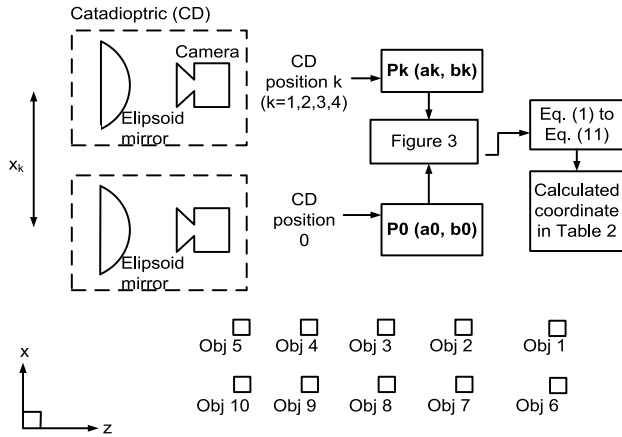
FIGURE 2. Illustration of the verification process. Ten square objects are located in front of the CD. Object images are captured by the CD in the two CD location.

TABLE 1. Position of the object relative to the CD position 0.

Object	Object position (mm)		
	x	y	z
Obj 1	425	150	2267
Obj 2	425	150	1767
Obj 3	425	150	1267
Obj 4	425	150	767
Obj 5	425	150	267
Obj 6	1315	150	2267
Obj 7	1315	150	1767
Obj 8	1315	150	1267
Obj 9	1315	150	767
Obj 10	1315	150	267

positions are given in Table 1. The value in Table 1 refers to the mirror center (its position is defined as CD Position 0). The square object is placed in the dark background to contrast the image. In this condition, the objects (white color) are clearly different from their background/environment (black color), so the image processing algorithm can easily detect the object. This condition imitates the thermal fault condition in the field, where the thermal fault appears as a white object (due to its higher temperature) while the surroundings appear black.

Also, in Figure 2, one pair of images of each object is required to calculate the approximate coordinates of an object. The first image is obtained when the camera is at the "CD position 0" location (0, 150, 0) in mm units. On the other hand, the second image is obtained when the CD is at "CD position k" (k=1, 2,3, 4) with coordinates (100,150,0) for "CD position 1", (200,150,0) for "CD position 2", (300,150,0) for "CD position 3", (400,150,0) for "CD position 4". The first image, P0, and the second image, Pk (k=1, 2, 3, 4), contain the images of ten verification objects where P0 has the coordinate set a and b as (a0,b0) and Pk has the coordinate set a and b as (ak,bk). P0 and Pk values are calculated from the midpoint of the image plane.

The values of P0 and Pk are then displayed in a single image to determine the object's actual coordinates, as shown in Figure 3. In Figure 3, measurements were made for four

pairs of CD locations (as illustrated in Figure 2). The first pair is for "CD position 0" and "CD position 1", with the x_k value being 100mm (Figure 3(a)). The second pair is "CD position 0" and "CD position 2", with the x_k value being 200mm (Figure 3(b)), and so on for pair three and pair four where the x_k values are x_k =300mm (Figure 3(c)) and x_k =400mm (Figure 3(d)). The blue dots in Figure 3 are the coordinates of a and b for the "CD position 0" (P0), while the red cross marks are the a and b coordinates for the "CD position 1" to "CD position 4" (Pk).

Furthermore, the coordinates P0 and Pk, according to Figure 3 of each object, are then entered into equations (1) to (11) to calculate the object's approximate location relative to CD. The calculation result of the object's approximate location with its percentage error (PE) is given in Table 2, while the correlation between error and fault distance as well as the other error analysis, is given in Table 3. The PE is the difference between the calculated coordinate and the actual coordinate, which is then divided by the actual coordinate for each of the x, y, and z coordinates. The MAPE, MAE, RMSE, and SD are the mean absolute percentage error, the mean absolute error, the root mean square error, and the standard deviation of absolute percentage error (APE).

1) ERROR CHARACTERISTIC

The deviation data of the measurement results in Table 2 is then processed to find the correlation between the object coordinate and the PE. Also, the MAPE, MAE, RMSE, and SD with the result as given in Table 3. The PE value is processed from Table 2 and plotted to see the APE distribution with the results shown in Figure 4.

Table 3 shows that the correlation between object distance and PE values is inconsistent, so no pattern of PE changes to changes in object distance can be found. The proposed method has a MAPE value below 6% for the x and z directions and around 70% for the y direction. This error value occurs because of the image processing technique's object detection process. In performing image processing, object detection is carried out based on the color difference of the object, which is then determined by the centroid value based on the average length of the detected object perimeter points. However, the non-linearity of CD projection affects the centroids' value determination. The centroid value from the image plane is then used as a and b values in the x and y-coordinate. Based on the experimental results, the 10 pixel error in determining the centroids can produce a distance prediction error of 5%. Even though the MAPE in the y direction has a large enough value, the SD of APE in the x, y, and z directions is less than 8%. It shows a consistency of measurement error over a reasonably small range, so the proposed method has good precision in the z, y, and z directions but has good accuracy only in the x and z directions. In addition, Figure 4(a) shows the distribution of the APE for the x, y, and z coordinates with the x_k value of 100mm. Figures 4(b) to Figure 4(d) show the same thing but for different x_k values, namely 200mm, 300mm, and 400mm, respectively.

TABLE 2. Object coordinate and error value. The actual coordinate is the real coordinate value of the verification object. The calculated coordinate is the predicted coordinate from the proposed method. Error is the deviation from the calculated coordinate and actual coordinate divided by the actual coordinate.

x_k (mm)	Actual coordinate (mm)			Calculated coordinate (mm)			PE (%)		
	x	y	z	x	y	z	x	y	z
100	425	150	2267	450.00	136.60	2278.39	5.88	-8.93	0.50
	425	150	1767	438.08	120.28	1718.82	3.08	-19.81	-2.73
	425	150	1267	444.00	138.64	1263.09	4.47	-7.57	-0.31
	425	150	767	442.03	151.63	770.41	4.01	1.08	0.44
	425	150	267	425.50	140.03	258.37	0.12	-6.65	-3.23
	1315	150	2267	1442.86	179.63	2438.08	9.72	19.75	7.55
	1315	150	1767	1199.90	65.29	1581.23	-8.75	-56.48	-10.51
	1315	150	1267	1266.22	102.66	1195.41	-3.71	-31.56	-5.65
	1315	150	767	1317.26	133.60	747.20	0.17	-10.94	-2.58
	1315	150	267	1284.48	122.40	246.42	-2.32	-18.40	-7.71
200	425	150	2267	438.64	119.40	2220.90	3.21	-20.40	-2.03
	425	150	1767	439.58	122.56	1724.69	3.43	-18.29	-2.39
	425	150	1267	448.79	146.02	1276.71	5.60	-2.66	0.77
	425	150	767	438.93	146.73	765.00	3.28	-2.18	-0.26
	425	150	267	426.39	141.46	258.91	0.33	-5.69	-3.03
	1315	150	2267	1191.83	53.56	2013.90	-9.37	-64.29	-11.16
	1315	150	1767	1256.65	94.15	1656.01	-4.44	-37.23	-6.28
	1315	150	1267	1301.61	120.76	1228.82	-1.02	-19.49	-3.01
	1315	150	767	1305.46	127.51	740.51	-0.73	-14.99	-3.45
	1315	150	267	1291.75	126.18	247.81	-1.77	-15.88	-7.19
300	425	150	2267	424.72	98.31	2150.39	-0.07	-34.46	-5.14
	425	150	1767	445.48	131.52	1747.85	4.82	-12.32	-1.08
	425	150	1267	444.83	139.92	1265.45	4.66	-6.72	-0.12
	425	150	767	436.88	143.51	761.43	2.79	-4.33	-0.73
	425	150	267	426.48	141.61	258.97	0.35	-5.59	-3.01
	1315	150	2267	1311.54	113.68	2216.19	-0.26	-24.21	-2.24
	1315	150	1767	1310.88	121.74	1727.48	-0.31	-18.84	-2.24
	1315	150	1267	1296.76	118.28	1224.24	-1.39	-21.15	-3.37
	1315	150	767	1306.92	128.27	741.34	-0.61	-14.49	-3.35
	1315	150	267	1291.82	126.21	247.83	-1.76	-15.86	-7.18
400	425	150	2267	428.33	103.78	2168.67	0.78	-30.81	-4.34
	425	150	1767	442.50	127.00	1736.17	4.12	-15.33	-1.74
	425	150	1267	444.60	139.58	1264.82	4.61	-6.95	-0.17
	425	150	767	435.59	141.48	759.19	2.49	-5.68	-1.02
	425	150	267	425.80	140.52	258.56	0.19	-6.32	-3.16
	1315	150	2267	1277.20	96.44	2158.17	-2.87	-35.71	-4.80
	1315	150	1767	1310.83	121.71	1727.42	-0.32	-18.86	-2.24
	1315	150	1267	1303.01	121.48	1230.15	-0.91	-19.01	-2.91
	1315	150	767	1302.96	126.23	739.09	-0.92	-15.85	-3.64
	1315	150	267	1293.94	127.31	248.23	-1.60	-15.12	-7.03

TABLE 3. Statistical analysis of model verification in CD prediction characteristic.

x_k	coordi nate	Correlations relationship between PE and object coordinate			MAPE (%)	MAE (mm)	RMSE (mm)	SD of APE (%)
		x	y	z				
100	x	0.23	-0.29	.793	4.22	39.91	58.62	3.03
	y	N/A	N/A	N/A	70.65	279.08	280.55	7.27
	z	.792	0.02	0.09	4.12	54.43	85.01	3.38
200	x	0.06	-0.58	.716	3.32	29.50	45.33	2.58
	y	N/A	N/A	N/A	68.31	269.83	271.13	6.72
	z	.681	-.658	0.24	3.96	55.62	91.10	3.16
300	x	-0.49	-0.35	0.41	1.70	11.10	13.86	1.72
	y	N/A	N/A	N/A	69.95	276.30	276.63	3.37
	z	-0.08	-.691	-0.22	2.85	32.88	45.89	2.01
400	x	-0.37	-0.42	0.54	1.88	13.89	17.30	1.49
	y	N/A	N/A	N/A	69.51	274.55	274.92	3.60
	z	0.23	-.767	-0.10	3.11	37.95	51.63	1.89

Compared with the method in [32] and [33], which is related to determining the geodetic objects using laser scanning (LiDAR), the results of this proposed method do have a more considerable error value. However, for the case of monitoring thermal disturbances in the PV, the LiDAR method cannot be used because it cannot differ the object with different temperatures (healthy and faulty module). The proposed method can provide early information to the operator about the appearance of the disturbance and an initial estimate of its location.

2) EFFECT OF x_k ON MAPE
In addition to the error distribution, the MAPE from Table 3 is then plotted against the x_k value change with the results

shown in Figure 5. Figure 5 shows that adding the x_k value can reduce the average error value for each coordinate. It can be used to determine the value of x_k used in field monitoring.

3) EFFECT OF x_k ON ERROR SENSITIVITY
The error sensitivity referred to here is the effect of the error on one axis on the other axes. Error sensitivity consists of the x-y, y-z, and x-z axes. The effect of x_k on the error sensitivity is given in Figure 6. Figure 6 represents the error sensitivity by the gradient error value. When the gradient is more significant, the influence of one axis on the other is also more significant. For example, for the x_k value of 100mm, the x-y gradient error value is 1.30, which means that an increase in the error of 1 unit on the x-axis can increase the error of 1.3 on the y-axis. In the measurement process, it is expected that errors on one axis do not cause a high increase in errors on the other axes.

In Figure 6, the X-Y gradient error experiences a different change pattern from the Y-Z and X-Z gradient errors. However, the overall gradient error tends to decrease as the value of x_k increases.

III. CASE STUDY
A. BACKGROUND
The utilization of large PV capacity is increasing in Indonesia. Difficulties monitoring thermal faults can occur in PV farms with large capacities, generally more than 1MWp. In this case study, we take the case of the monitoring model for the largest PV currently in Indonesia, namely Likupang PV farms. Likupang PV farm is located in Likupang village, North Sulawesi province, with a capacity of 21MWp covering an area of 29Ha. This PV farm is north of the equator, with a tilt angle of less than 10°, and points to the south. It is an overview of the thermal fault detection process in the PV system layout in the field. In addition, the case study also explored the most significant detection error that might occur if the proposed method is used in actual conditions, such as
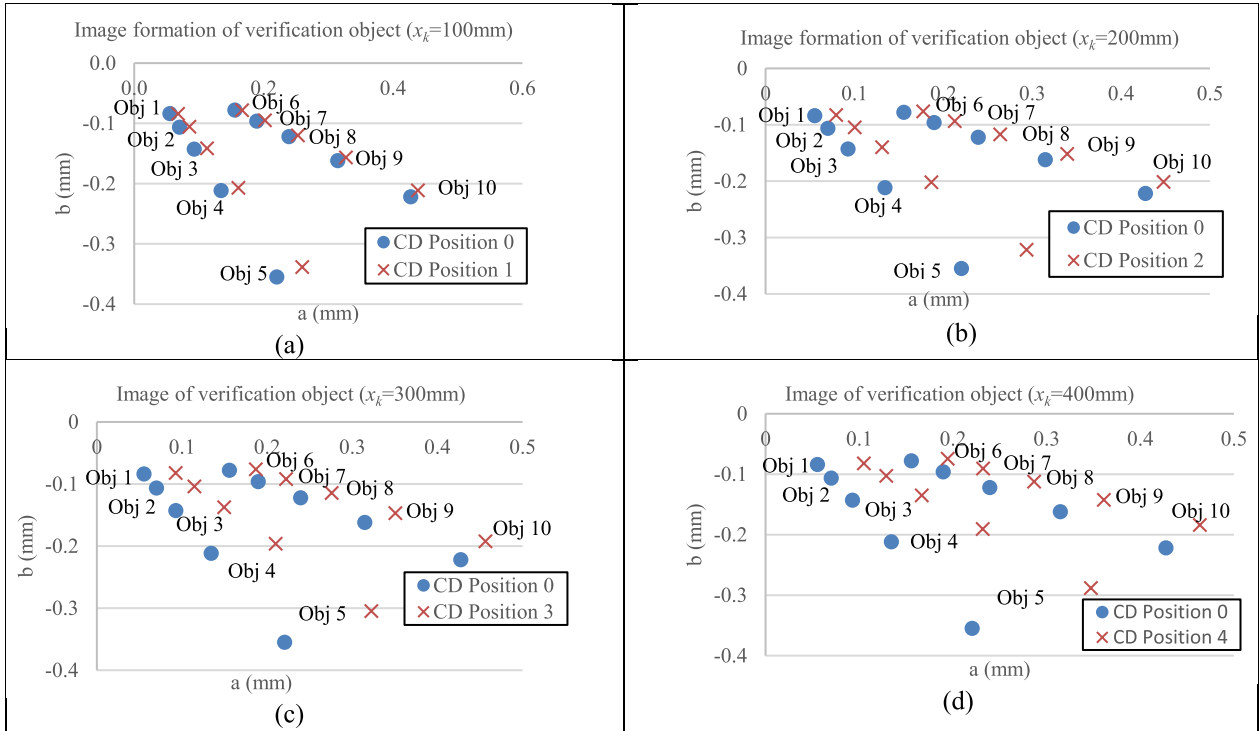
FIGURE 3. Value *a* and *b* of the image of ten verification objects when captured in two CD locations. (a) Image of verification object for CD position 0 and 1 (x_k = 100mm). (b) Image of verification object for CD position 0 and 2 (x_k = 200mm). (c) Image of verification object for CD position 0 and 3 (x_k = 300mm). (d) Image of verification object for CD position 0 and 4 (x_k = 400mm).
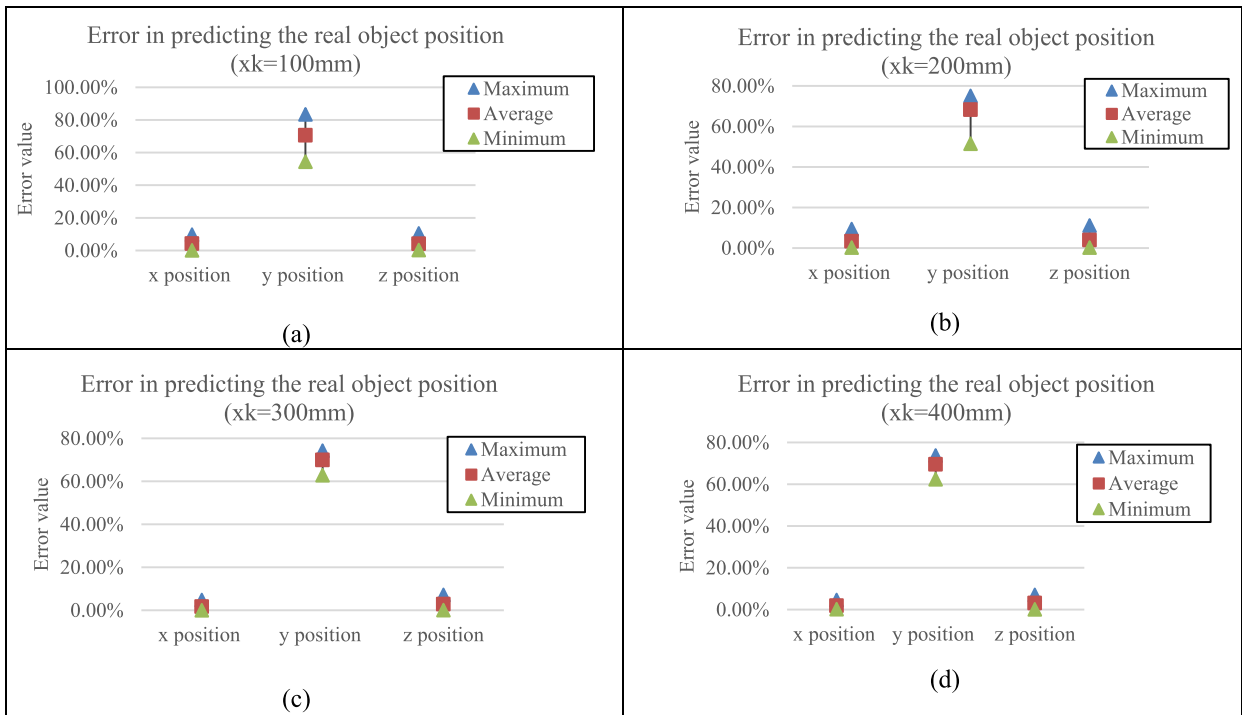

FIGURE 4. Error characteristic in predicting the actual object position based on verification result. Error is an absolute deviation of the calculation result and actual value and then divided by the actual value (APE). (a) Error characteristic for x_k = 100mm. (b) Error characteristic for x_k = 200mm. (c) Error characteristic for x_k = 300mm. (d) Error characteristic for x_k = 400mm.

in the Likupang PV system. The uncertainty area that occurs due to the prediction error can be estimated through the case study.

B. MONITORING SCHEME

The CD model developed has a viewing angle value of more than 90°, so for the Likupang PV monitoring model, 15 points
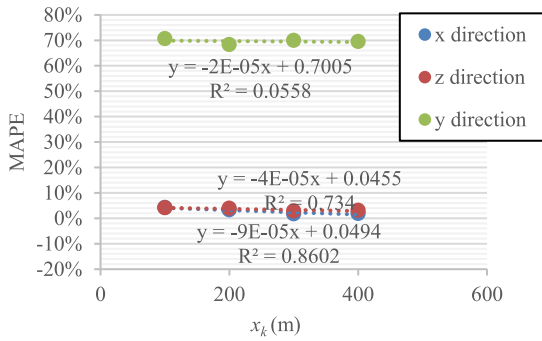
FIGURE 5. The MAPE values of x, y, and z coordinate for different x_k values.
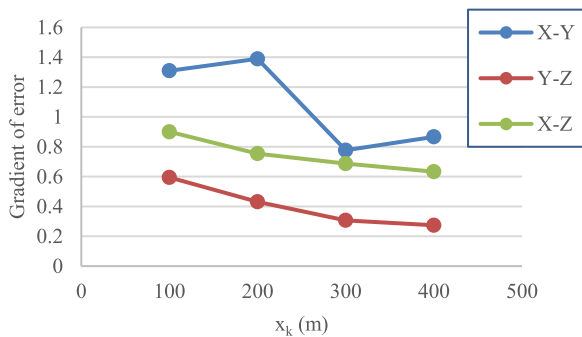

FIGURE 6. Effect of x_k in the error gradient of x-y, y-z, and x-z coordinate pair. The gradient of error tends to be reduced when the x_k increases.

of CD placement are used (with the height of $y = 15$m). The layout of the Likupang PV farm and the location of the CD placement is given in Figure 7. In this case, the PV's images on each CD were made using a simulator based on equations (1) and equation (2) [30], [31] where the simulation results are given in Figure 8. In the simulator, we made the disturbance points yellow, while The PV and other environmental areas are shown in blue and black.

The CD coordinates are given in Table 4 regarding the coordinates (0,0,0) located at the origin point in Figure 7. The location of this CD is chosen to ensure that the entire PV module can be monitored. Therefore, if a thermal fault occurs, the CD system can determine the location of the coordinates of the disturbance relative to the position of the CD that detects it. In this paper, we still place CDs based on the coverage area only so that there is a potential for two cameras to observe overlapping areas. In the future implementation phase in the field, we can adapt particle swarm optimization methods, such as [34], to determine the most effective and cost-efficient camera locations.

The entire CD set in Figure 7 has a point of view in the direction of the z-axis with no rotation angle in the direction of the x-axis and y-axis. Each CD device has two monitoring conditions: condition 1, when the monitoring location corresponds to the x, y, and z values in Table 4, and condition 2, when the x_k value reduces the x value in Table 4 by 1.5m with fixed y and z values.

In this case study, it is modelled that there are three thermal faults in each CD view, so there are 45 thermal faults overall in the PV farm. The thermal fault appearance for each CD view (condition 1) is marked as "Label=1", "Label=2", and "Label=3", as given in Figure 7.

Detecting thermal disturbances in the field is carried out using a thermal camera. Thermal cameras produce different images for objects with different temperatures, generally black for lower temperatures and white for higher temperatures. To imitate a thermal camera image, in this case study, the PV simulator gives a yellow color at the disturbance point, while healthy PV and other environmental areas are shown in blue and black. This image is then analyzed using image processing into a black-and-white monochrome form. Objects with white color are identified as thermal faults, then isolated to form a perimeter that covers the faulted object. After the object is detected, the center point (centroid) is determined. This midpoint is used as object image coordinates (a and b). Then, the a and b values are used in further calculations.

C. RESULT AND DISCUSSION

Based on the image coordinate of the thermal fault points in Figure 8, then by using the calculations in (1) to (11), the approximate value of the thermal fault coordinates relative to the CD that detects it is given in Table 5.

1) PREDICTION ERROR CHARACTERISTIC

Simulated coordinates of real conditions represent the actual coordinate conditions of the thermal disturbance, which use as the reference for error calculation. Positive values in determining the location of the x and z axes in Table 5 represent that the disturbance is to the left of the CD. At the same time, the negative value indicates that the disturbance is more to the right of the CD observation direction. For example, the values of x=−40.15m and z=60.79m (in the calculated result CD 1) indicate the disturbance is on the right side of CD 1 (with a distance of 40.15m). The disturbance is also located in front of CD, with a distance of 60.79m. When viewed from the origin coordinates (0,0,0) in Figure 6, the location of the disturbance in the direction of the x and the z-axis is equal to the coordinates CD minus the calculation result in Table 5. For CD 1, the fault coordinate from the origin is x-origin = 450 -(-40.15) = 490m and z-origin = 80 – 60.79=140.79m. The location of the coordinates to the origin for other thermal disturbances on CD 2 to CD 15 was determined using the same method. The error values in Table 5 are presented on the graph in Figure 9 to provide a visual characteristic of the error value to the distance of the disturbance point. Figure 9 only shows the coordinate value data for the x-axis and z-axis directions because, based on the verification results in Figure 4 and Figure 5, this method is inaccurate in detecting the y-axis coordinates.

Figure 9 shows that the error value of the x and z directions is less than ±10%. Some statistical analysis was performed to explore the error characteristic. A correlation (between PE and object coordinates), MAPE, MAE, and RMSE analysis
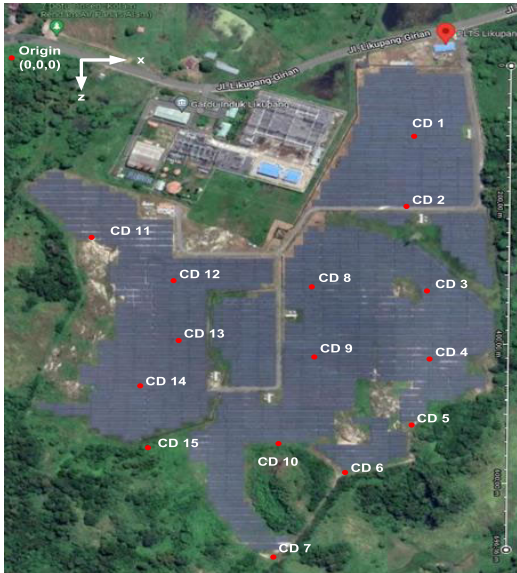
FIGURE 7. Lay out of the Likupang PV farm [35] and the CD position. There are 15 CDs used to monitor all of the PV farms. The location of CDs is chosen to cover all PV modules.

TABLE 4. CD coordinate is relative to the origin position, as given in Figure 7.

CD Number	CD coordinate		
	x (m)	y (m)	z (m)
1	450	15	80
2	440	15	210
3	460	15	330
4	470	15	440
5	445	15	520
6	370	15	590
7	290	15	705
8	320	15	340
9	320	15	430
10	320	15	520
11	75	15	250
12	160	15	340
13	160	15	420
14	150	15	490
15	130	15	555

TABLE 5. Image coordinates based on calculation and simulation. The calculated coordinate (CC) is the predicted coordinate from the proposed method. The simulated coordinate of real condition (SC) is the simulated actual coordinate value of the thermal fault in the PV farm. Error (PE) is the deviation from the CC and SC and is divided by SC.

Catadioptric (CD) position	Calculated coordinate		Simulated coordinate of the real condition		PE	
	x (m)	z (m)	x (m)	z (m)	x (%)	z (%)
CD 1	-40.15	60.79	-40	60	0.38	1.32
	30.81	60.64	30	60	2.70	1.06
	53.96	59.99	53	60	1.81	-0.02
CD 2	-48.68	29.19	-50	30	-2.64	-2.72
	21.28	72.97	20	70	6.40	4.24
	42.42	58.51	43	60	-1.36	-2.48
CD 3	-32.14	86.75	-30	80	7.14	8.44
	42.20	62.68	40	60	5.50	4.46
	60.52	37.87	63	40	-3.93	-5.32
CD 4	-20.89	95.30	-20	90	4.47	5.89
	72.54	40.82	70	40	3.63	2.05
	97.54	53.31	90	50	8.38	6.62
CD 5	-25.42	54.33	-24	51	5.91	6.52
	5.18	39.39	5	40	3.59	-1.54
	16.40	53.48	15	50	9.32	6.96
CD 6	-14.77	19.79	-15	20	-1.57	-1.06
	51.08	60.30	50	60	2.16	0.50
	106.25	62.50	100	60	6.25	4.17
CD 7	35.92	51.16	38	55	-5.48	-6.99
	40.03	45.53	39	45	2.63	1.17
	39.53	24.33	40	25	-1.17	-2.70
CD 8	-74.40	96.20	-70	90	6.29	6.88
	-19.72	60.00	-20	60	-1.41	0.00
	56.96	19.22	58	20	-1.79	-3.90
CD 9	-65.78	65.78	-70	70	-6.03	-6.02
	-19.42	49.14	-20	50	-2.90	-1.71
	59.38	30.18	58	30	2.38	0.59
CD 10	-29.77	19.85	-30	20	-0.76	-0.76
	-74.40	96.20	-70	90	6.29	6.88
	58.97	40.01	58	40	1.67	0.01
CD 11	10.87	73.45	10	70	8.69	4.93
	25.28	59.49	25	60	1.10	-0.85
	37.12	52.22	35	50	6.06	4.45
CD 12	-69.92	19.87	-70	20	-0.11	-0.65
	-61.00	30.48	-60	30	1.66	1.60
	56.81	37.30	60	40	-5.32	-6.74
CD 13	-65.89	56.83	-70	60	-5.87	-5.28
	-41.31	45.99	-45	50	-8.20	-8.02
	38.65	38.09	40	40	-3.37	-4.78
CD 14	-91.83	27.43	-100	30	-8.17	-8.57
	-56.08	61.63	-55	60	1.96	2.71
	30.00	87.22	30	90	0.00	-3.09
CD 15	-74.79	18.61	-80	20	-6.51	-6.95
	-73.00	38.89	-75	40	-2.66	-2.78
	9.77	70.03	10	75	-2.26	-6.62

was carried out, as given in Table 6. Correlation analysis showed no consistency in the correlation value between the disturbance distance and the PE value, which aligns with the results in Table 3. The MAE and RMSE values are less than 5m.

A MAPE of less than 6% in the x- and z directions for objects 100m away gives an area of uncertainty of 144m^2. In addition to errors in the x-axis and z-axis directions, the y-axis error does have a relatively large percentage of error. However, for PV monitoring implementation conditions, the highest distance of the panel from the ground (y-axis direction) is generally less than 3m. The y-axis direction error is only in that range because the fault only appears on the PV module, so the MAPE value of 14% (0.5m error) is reasonable. Also, the MAE and RMSE values less than 5m

are still good enough to be used as an initial estimate by the operator to detect the disturbance area.

As shown in Figure 8, the proposed method can label the fault location, and each fault's coordinates (a and b) is not be swapped. Therefore, detecting multiple faults in one CD view is not an issue. Also, because the detection process relies on a and b values, the accuracy value of the prediction process is not affected by the number of disturbances observed by one CD.
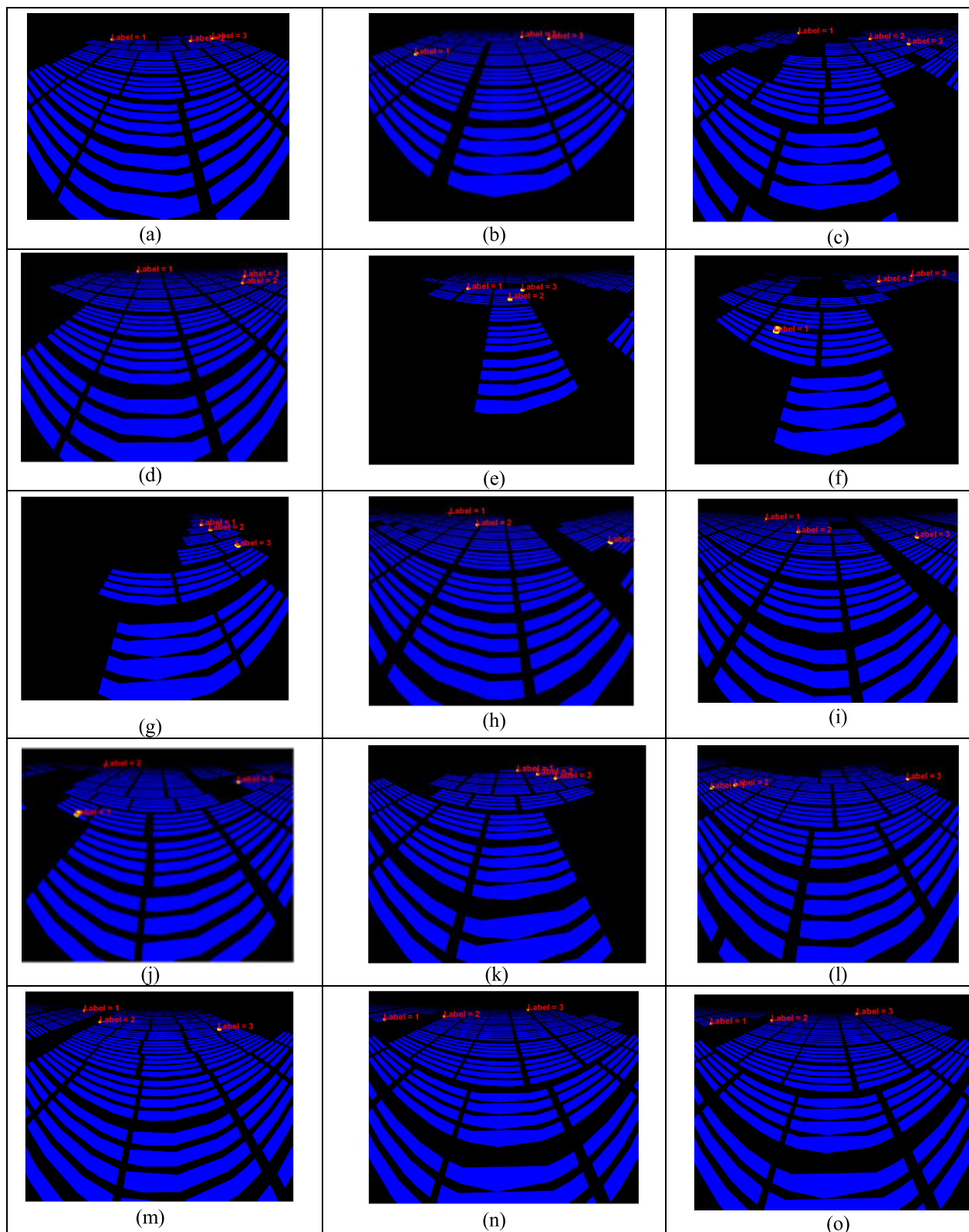
FIGURE 8. Simulation of PV farm monitoring using CD. It is simulated that the PV module experience thermal faults, and the CD detects the fault location based on the proposed method. (a) The image perspective of PV farm from CD 1. (b) The image perspective of PV farm from CD 2. (c) The image perspective of PV farm from CD 3. (d) The image perspective of PV farm from CD 4. (e) The image perspective of PV farm from CD 5. (f) The image perspective of PV farm from CD 6. (g) The image perspective of PV farm from CD 7. (h) The image perspective of PV farm from CD 8. (i) The image perspective of PV farm from CD 9. (j) The image perspective of PV farm from CD 10. (k) The image perspective of PV farm from CD 11. (l) The image perspective of PV farm from CD 12. (m) The image perspective of PV farm from CD 13. (n) The image perspective of PV farm from CD 14. (o) The image perspective of PV farm from CD 15.
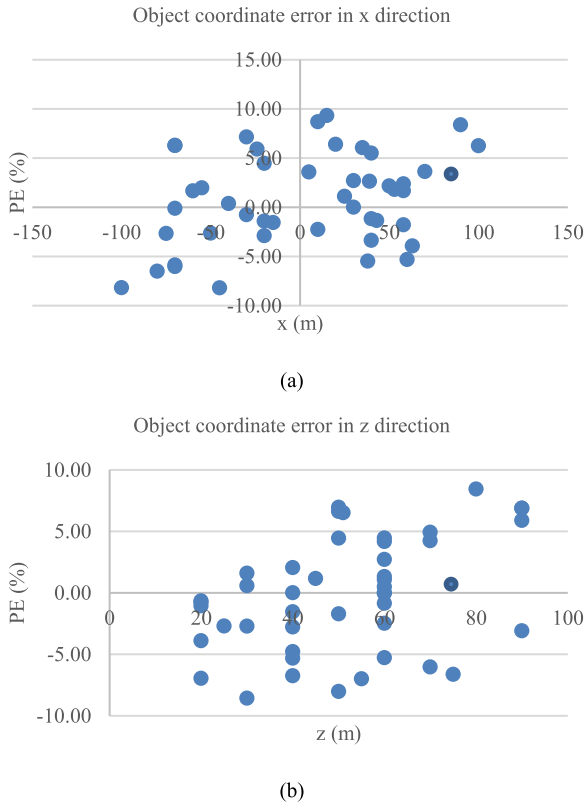
(a)

(b)

FIGURE 9. Error value (PE) of object position. (a) Error characteristic in the x direction. (b) Error characteristic in the z-direction.

Coordinate detection of the *x* and *z* direction can provide a fast overview of the thermal fault location required by the operator. Therefore, the operator can perform more detailed checks on the small area inside the error range of the *x* and *z* directions. This method makes determining the location of disturbances faster and speeds up fault management planning.

2) SENSITIVITY PATTERN

CD is expected to have good health in the disturbance monitoring process. For this reason, the sensitivity pattern can be used to indicate CD equipment condition. The sensitivity pattern is a profile of the error value relationship between the x, y, z directions. In this case study, the CD used has a sensitivity pattern profile, according to Figure 10.

Figures 10 (a) to 10 (c) shows the sensitivity patterns in the *x* and *y*, *x* and *z*, and *y* and *z* directions, respectively. The sensitivity pattern can be approximated by linear regression with a relationship value of $R^2 > 0.9$. CD condition calibration can be performed by comparing the measured sensitivity pattern value with the sensitivity pattern reference in Figure 10. If it turns out that the R^2 sensitivity pattern obtained from the prediction results is much smaller than the reference value, then it can be indicated that the prediction results from the CD are invalid or the CD is damaged.

In the future, besides detecting disturbances, the prognosis of thermal fault disturbances needs to be considered. The
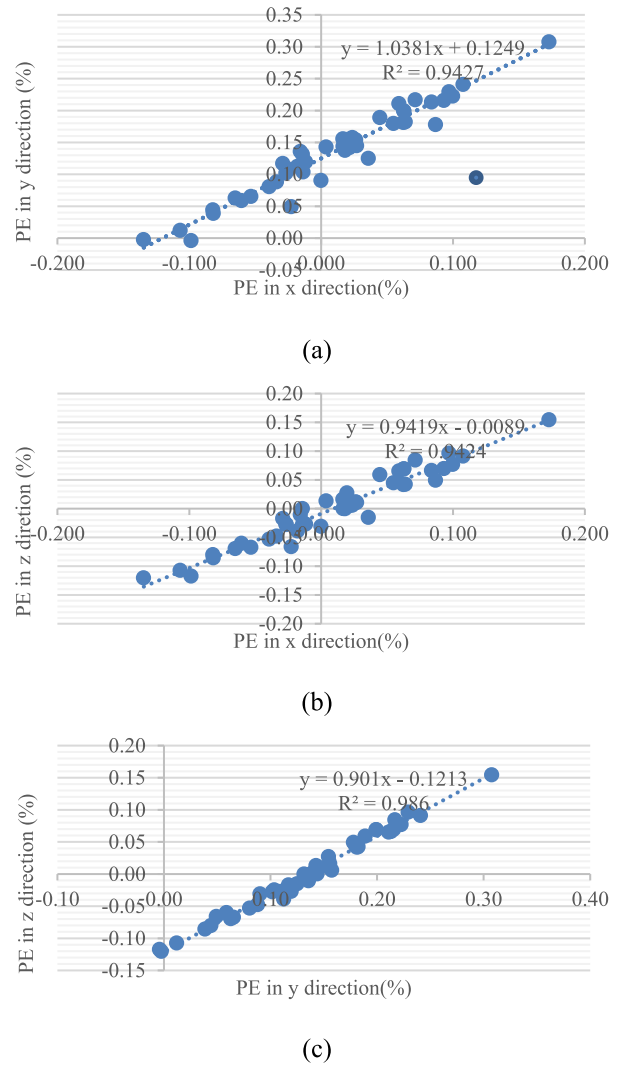

(a)

(b)

(c)

FIGURE 10. Sensitivity pattern of CD. (a) sensitivity pattern of x and y error values. (b) sensitivity pattern of x and z error values. (c) sensitivity pattern of y and z error values.

TABLE 6. Statistical analysis of case study in CD prediction characteristic.

coordi nate	Correlations relationship between PE and object coordinate			MAPE (%)	MAE (m)	RMSE (m)
	x	y	z			
x	.239	-.172	.158	5.26	2.499	3.539
y	N/A	N/A	N/A	13.67	1.908	2.128
z	-.054	-.258	-.616**	5.03	2.937	3.918

process of fault prognosis using the multistage fault method involving Bayesian networks and autoregressive moving averages describes in [36]. This method can adequately track the degradation process of the permanent magnet synchronous generator. In addition, dynamic Bayesian networks are also used to diagnose disturbances through multiple modular redundant closed-loop feedback, sensor data, and system parameters. This method can detect disturbances with high

accuracy in cases of subsea blowout preventer systems [37]. This method can potentially be used in the prognosis and fault detection in PV, complementing the proposed method's performance.

IV. CONCLUSION

Thermal faults are disturbances that frequently occur in PV, harm efficiency, and initiate accelerating aging of the PV module. Therefore, a detection system that can work continuously and quickly provide predictions of fault locations is needed. CD is prospective to solve this problem because it has a wide viewing angle in detecting disturbances. With the detection model that has been built, the CD can predict fault locations with reasonable error values. The parameter x_k tends to affect the average measurement error of the coordinate prediction and the error gradient of each axes couple. Greater the x_k, smaller measurement and gradient error can be achieved. In addition, the case study simulation result shows that the thermal fault position can be predicted with the worst PE of less than 10%, with a MAPE, MAE, and RMSE in a reasonable value. Also, the sensitivity pattern can be used for CD condition monitoring. Future work is needed to increase the prediction accuracy by improving the image processing technique to detect the centroids of the thermal faults.

ACKNOWLEDGMENT

REFERENCES

[1] E. Asmelash and G. Prakash. *Future of Solar Photovoltaic: Deployment, Investment, Technology, Grid Integration and Socio-Economic Aspects (A Global Energy Transformation: Paper)*. International Renewable Energy Agency, Abu Dhabi, Uni Arab Emirates. Accessed: Feb. 10, 2022. [Online]. Available: https://irena.org/-/media/Files/IRENA/Agency/Publication/2019/Nov/IRENA_Future_of_Solar_PV_2019

[2] S. R. Madeti and S. N. Singh, "Monitoring system for photovoltaic plants: A review," *Renew. Sustain. Energy Rev.*, vol. 67, pp. 1180–1207, Jan. 2017.

[3] V. Benda and L. Černá, "PV cells and modules—State of the art, limits and trends," *Heliyon*, vol. 6, no. 12, Dec. 2020, Art. no. e05666.

[4] M. M. Escribano, M. G. Solano, I. de la Parra Laita, J. M. Alvarez, L. Marroyo, and E. L. Pigueiras, "Module temperature dispersion within a large PV array: Observations at the amareleja PV plant," *IEEE J. Photovolt.*, vol. 8, no. 6, pp. 1725–1731, Nov. 2018.

[5] A. Mellit, G. M. Tina, and S. A. Kalogirou, "Fault detection and diagnosis methods for photovoltaic systems: A review," *Renew. Sustain. Energy Rev.*, vol. 91, pp. 1–17, Aug. 2018.

[6] Y. Zhang, Y. Yu, F. Meng, and Z. Liu, "Experimental investigation of the shading and mismatch effects on the performance of bifacial photovoltaic modules," *IEEE J. Photovolt.*, vol. 10, no. 1, pp. 296–305, Jan. 2020.

[7] S. Kawai, T. Tanahashi, Y. Fukumoto, F. Tamai, A. Masuda, and M. Kondo, "Causes of degradation identified by the extended thermal cycling test on commercially available crystalline silicon photovoltaic modules," *IEEE J. Photovolt.*, vol. 7, no. 6, pp. 1511–1518, Nov. 2017.

[8] S. S. Nair, "A survey report of the firefighters on fire hazards of PV fire," in *Proc. IEEE Int. Conf. Syst., Comput., Autom. Netw. (ICSCA)*, Jul. 2018, pp. 1–5.

[9] A. Triki-Lahiani, A. B.-B. Abdelghani, and I. Slama-Belkhodja, "Fault detection and monitoring systems for photovoltaic installations: A review," *Renew. Sustain. Energy Rev.*, vol. 82, pp. 2680–2692, Feb. 2018.

[10] S. Vergura and F. Marino, "Quantitative and computer-aided thermography-based diagnostics for PV devices: Part I—Framework," *IEEE J. Photovolt.*, vol. 7, no. 3, pp. 822–827, May 2017.

[11] P. B. Quater, F. Grimaccia, S. Leva, M. Mussetta, and M. Aghaei, "Light unmanned aerial vehicles (UAVs) for cooperative inspection of PV plants," *IEEE J. Photovolt.*, vol. 4, no. 4, pp. 1107–1113, Jul. 2014.

[12] S. Deng, Z. Zhang, C. Ju, J. Dong, Z. Xia, X. Yan, T. Xu, and G. Xing, "Research on hot spot risk for high-efficiency solar module," *Energy Proc.*, vol. 130, pp. 77–86, Sep. 2017.

[13] P.-Y. Sevilla-Camacho, M.-A. Zuniga-Reyes, J.-B. Robles-Ocampo, R. Castillo-Palomera, J. Muniz, and J. Rodriguez-Resendiz, "A novel fault detection and location method for PV arrays based on frequency analysis," *IEEE Access*, vol. 7, pp. 72050–72061, 2019.

[14] Y. He, B. Du, and S. Huang, "Noncontact electromagnetic induction excited infrared thermography for photovoltaic cells and modules inspection," *IEEE Trans. Ind. Informat.*, vol. 14, no. 12, pp. 5585–5593, Dec. 2018.

[15] T. Takashima, J. Yamaguchi, K. Otani, T. Oozeki, K. Kato, and M. Ishida, "Experimental studies of fault location in PV module strings," *Sol. Energy Mater. Sol. Cells*, vol. 93, nos. 6–7, pp. 1079–1082, Jun. 2009.

[16] A. Y. Appiah, X. Zhang, B. B. K. Ayawli, and F. Kyeremeh, "Review and performance evaluation of photovoltaic array fault detection and diagnosis techniques," *Int. J. Photoenergy*, vol. 2019, pp. 1–19, Feb. 2019.

[17] Z. Yi and A. H. Etemadi, "Line-to-line fault detection for photovoltaic arrays based on multiresolution signal decomposition and two-stage support vector machine," *IEEE Trans. Ind. Electron.*, vol. 64, no. 11, pp. 8546–8556, Nov. 2017.

[18] A. Salazar and E. Q. Macabebe, "Hotspots detection in photovoltaic modules using infrared thermography," in *Proc. MATEC Web Conf.*, 2016, p. 10015.

[19] Y. Hu, W. Cao, J. Ma, S. J. Finney, and D. Li, "Identifying PV module mismatch faults by a thermography-based temperature distribution analysis," *IEEE Trans. Device Mater. Rel.*, vol. 14, no. 4, pp. 951–960, Dec. 2014.

[20] Y. Hu, W. Cao, J. Wu, B. Ji, and D. Holliday, "Thermography-based virtual MPPT scheme for improving PV energy efficiency under partial shading conditions," *IEEE Trans. Power Electron.*, vol. 29, no. 11, pp. 5667–5672, Nov. 2014.

[21] M. Libra, M. Daneček, J. Lešetický, V. Poulek, J. Sedláček, and V. Beránek, "Monitoring of defects of a photovoltaic power plant using a drone," *Energies*, vol. 12, no. 5, p. 795, Feb. 2019.

[22] C. Henry, S. Poudel, S.-W. Lee, and H. Jeong, "Automatic detection system of deteriorated PV modules using drone with thermal camera," *Appl. Sci.*, vol. 10, no. 11, p. 3802, May 2020.

[23] D. Rossi, M. Omaña, D. Giaffreda, and C. Metra, "Modeling and detection of Hotspot in shaded photovoltaic cells," *IEEE Trans. Very Large Scale Integr. (VLSI) Syst.*, vol. 23, no. 6, pp. 1031–1039, Jun. 2015.

[24] S. Chattopadhyay, R. Dubey, S. Bhaduri, S. Zachariah, H. K. Singh, C. S. Solanki, A. Kottantharayil, N. Shiradkar, B. M. Arora, K. L. Narasimhan, and J. Vasi, "Correlating infrared thermography with electrical degradation of PV modules inspected in all-India survey of photovoltaic module reliability 2016," *IEEE J. Photovolt.*, vol. 8, no. 6, pp. 1800–1808, Nov. 2018.

[25] E. L. Meyer and E. E. van Dyk, "Assessing the reliability and degradation of photovoltaic module performance parameters," *IEEE Trans. Rel.*, vol. 53, no. 1, pp. 83–92, Mar. 2004.

[26] D. P. Winston, "Efficient output power enhancement and protection technique for hot spotted solar photovoltaic modules," *IEEE Trans. Device Mater. Rel.*, vol. 19, no. 4, pp. 664–670, Dec. 2019.

[27] A. Y. Appiah, X. Zhang, B. B. K. Ayawli, and F. Kyeremeh, "Long short-term memory networks based automatic feature extraction for photovoltaic array fault diagnosis," *IEEE Access*, vol. 7, pp. 30089–30101, 2019.

[28] W. Gao and R.-J. Wai, "A novel fault identification method for photovoltaic array via convolutional neural network and residual gated recurrent unit," *IEEE Access*, vol. 8, pp. 159493–159510, 2020.

[29] K. H. Choi, Y. Kim, and C. Kim, "Analysis of fish-eye lens camera self-calibration," *Sensors*, vol. 19, no. 5, pp. 1424–8220, Mar. 2019.

[30] C. Geyer and K. Daniilidis, "Catadioptric projective geometry," *Int. J. Comput. Vis.*, vol. 45, no. 3, pp. 223–243, 2001.

[31] X. Ying and Z. Hu, "Can we consider central catadioptric cameras and fisheye cameras within a unified imaging model?" in *Computer Vision—ECCV 2004* (Lecture Notes in Computer Science), vol. 3021, T. Pajdla and J. Matas, Eds. Berlin, Germany: Springer, 2004, doi: 10.1007/978-3-540-24670-1_34.

[32] M. Cateanu, "LiDAR for ground surface mapping in forest environments," *Young Scientist*, vol. V, pp. 173–178, 2017. [Online]. Available: https://www.researchgate.net/publication/345759911_LIDAR_FOR_GROUND_SURFACE_MAPPING_IN_FOREST_ENVIRONMENTS

[33] C. L. Glennie, W. E. Carter, R. L. Shrestha, and W. E. Dietrich, "Geodetic imaging with airborne LiDAR: The Earth's surface revealed," *Rep. Prog. Phys.*, vol. 76, no. 8, Aug. 2013, Art. no. 086801.

[34] X. Kong, B. Cai, Y. Liu, H. Zhu, Y. Liu, H. Shao, C. Yang, H. Li, and T. Mo, "Optimal sensor placement methodology of hydraulic control system for fault diagnosis," *Mech. Syst. Signal Process.*, vol. 174, Jul. 2022, Art. no. 109069.

[35] Google. *PLTS Likupang*. Accessed: May 20, 2022. [Online]. Available: https://goo.gl/maps/JXZqZYLYmyBPthPa7

[36] B. Cai, Z. Wang, H. Zhu, Y. Liu, K. Hao, Z. Yang, Y. Ren, Q. Feng, and Z. Liu, "Artificial intelligence enhanced two-stage hybrid fault prognosis methodology of PMSM," *IEEE Trans. Ind. Informat.*, vol. 18, no. 10, pp. 7262–7273, Oct. 2022.

[37] X. Kong, B. Cai, Y. Liu, H. Zhu, C. Yang, C. Gao, Y. Liu, Z. Liu, and R. Ji, "Fault diagnosis methodology of redundant closed-loop feedback control systems: Subsea blowout preventer system as a case study," *IEEE Trans. Syst., Man, Cybern. Syst.*, early access, Sep. 20, 2022, doi: 10.1109/TSMC.2022.3204777.

RINALDY DALIMI was born in Tanjung Pinang, Indonesia. He received the B.S. degree in electrical engineering from the Universitas Indonesia, Depok, Indonesia, in 1980, the M.Sc. degree in control system from the Michigan State University, MI, USA, in 1988, and the Ph.D. degree in power system from the Virginia Polytechnic Institute and State University, VA, USA, in 1992. Since 1985, he has been a Lecturer with the Universitas Indonesia, where he was the Dean of the Engineering Faculty, from 2004 to 2008. From 2009 to 2019, he was a member of the National Energy Council of Indonesia, which has main responsibility to formulate national energy policy. He is currently a Professor with the Department of Electrical Engineering, Faculty of Engineering, Universitas Indonesia. He has authored or coauthored several journals and IEEE proceeding publications. His current research interests include power systems, renewable energy and energy management, and economic. He is an active reviewer for many reputed journals and letters.

• • •

PUTU AGUS ADITYA PRAMANA was born in Gianyar, Indonesia. He received the B.Eng. degree in engineering physics and the M.Eng. degree in instrumentation and control from the Faculty of Industrial Technology, Institut Teknologi Bandung, in 2012 and 2014, respectively. He is currently pursuing the Ph.D. degree with the Department of Electrical Engineering, Universitas Indonesia. In 2015, he joined PT PLN (Persero), an Indonesian National Electricity Company. Currently, he is a Researcher with PT PLN (Persero), Research Institute. He has authored or coauthored a dozen papers published in refereed journals and conferences. His research interests include power system operation, control systems, and renewable energy.